Determination of the process-induced microstructure of woven glass fabric reinforced polyamide 6.6/6 composite using terahertz pulsed imaging

J. Calvo-de la Rosa, Pascal Pomarède, P. Antonik, Fodil Meraghni, D.S. Citrin, D. Rontani, A. Locquet

▶ **To cite this version:**

J. Calvo-de la Rosa, Pascal Pomarède, P. Antonik, Fodil Meraghni, D.S. Citrin, et al.. Determination of the process-induced microstructure of woven glass fabric reinforced polyamide 6.6/6 composite using terahertz pulsed imaging. NDT & E International, 2023, 136, pp.102799. 10.1016/j.ndteint.2023.102799 . hal-04037541

HAL Id: hal-04037541
https://hal.science/hal-04037541

Submitted on 20 Mar 2023

HAL is a multi-disciplinary open access archive for the deposit and dissemination of scientific research documents, whether they are published or not. The documents may come from teaching and research institutions in France or abroad, or from public or private research centers.

L'archive ouverte pluridisciplinaire **HAL**, est destinée au dépôt et à la diffusion de documents scientifiques de niveau recherche, publiés ou non, émanant des établissements d'enseignement et de recherche français ou étrangers, des laboratoires publics ou privés.

Determination of the process-induced microstructure of woven glass fabric reinforced polyamide 6.6/6 composite using terahertz pulsed imaging

J. Calvo-de la Rosa [a,b,c,*], P. Pomarède [a,e], P. Antonik [b], F. Meraghni [e], D.S. Citrin [a,d], D. Rontani [b], A. Locquet [a,d]

[a] Georgia Tech-CNRS IRL 2958, Georgia Tech Europe, 2 Rue Marconi, 57070, Metz, France
[b] Chair in Photonics, LMOPS EA 4423 Laboratory, CentraleSupélec & Université de Lorraine, 2 rue Edouard, Belin, F-57070, Metz, France
[c] Department of Condensed Matter Physics, Faculty of Physics, Universitat de Barcelona, Martí i Franquès 1 08028, Barcelona, Spain
[d] School of Electrical and Computer Engineering, Georgia Institute of Technology, Atlanta, GA, 30332-0250, USA
[e] Arts et Métiers Institute of Technology, CNRS, Université, de Lorraine, LEM3-UMR 7239 CNRS, 4 rue Augustin Fresnel, 57078, Metz, France

A B S T R A C T

Terahertz pulsed imaging, combined with spatial and temporal signal and image processing, is performed to visualize the woven fabric in the various plies of glass-fiber-reinforced polymer laminates and to determine quantitative parameters characterizing the microstructure such as fiber-bundle orientation and the distance between yarns. The results are in quantitative agreement with the microstructure features provided by the manufacturer. In addition, the employed signal processing shows an excellent capability to reveal the weave pattern from noisy C-scans - where a visual-based analysis can be problematic - and to assess the process-induced microstructure.

1. Introduction

The growing need to replace metals with strong and stiff lightweight materials with other desirable mechanical, thermal, and chemical properties has led to the development of a range of composite materials. Among these, woven glass-fiber-reinforced polymer (GFRP) laminates are currently employed in high-impact sectors such as aeronautics [1–3], automotive [4,5], renewable energy [6,7], and civil engineering [8,9]. In addition to a favorable density/strength relationship and significant resistance to impact, GFRPs are also low-cost composites [10], in contrast to, for example, carbon-fiber-reinforced polymers (CFRP).

GFRP's properties arise from the combination of the low density of the polymer matrix and the high strength provided by the glass fibers. There exist multiple arrangements depending on the fibers' characteristics (length or width, for instance) and how they are spatially distributed [1,11]. Glass fibers can be randomly oriented in the polymeric matrix, leading to a transversely isotropic material. Another approach consists of unidirectionally oriented fiber resulting in an improved mechanical response in the direction of the fibers. This anisotropy makes these materials useful for applications where the stress direction is constant and well known. There are also composites in which fiber bundles (yarns or tows) are woven into fabrics, mixed with a polymer in thin plies, and stacked together, forming a multilayered woven laminate [1]. It improves mechanical properties ranging from orthotropic to quasi-isotropic depending on the chosen stacking sequence. Consequently, this type of GFRP is most commonly used for structural elements in demanding applications. Therefore, accurate knowledge of the composite's microstructure is vital to rely on its mechanical capabilities. This study focuses on such GFRP laminates incorporating woven glass-fiber fabrics in a thermoplastic matrix. As for all composite types, the physical characteristics of the fibers (diameter, length, orientation, concentration, bundle structure and weave pattern) play a crucial role in the determination of the mechanical behavior of the composite [8,11].

When these materials are used for critical components (such as structural components in aircrafts), it becomes crucial to test them both in production and service [6,12]. Regarding production, a proper quality-control process is essential to confirm that the produced GFRP laminate has the desired microstructure and that there are no significant defects before being deployed as a load-bearing component. For in-service testing, routine evaluation may be required to detect the presence of damage that may lead to the component's failure. There are

* Corresponding author. Georgia Tech-CNRS IRL2958, Georgia Tech Lorraine, 2 Rue Marconi, 57070, Metz, France.
E-mail address: jaumecalvo@ub.edu (J. Calvo-de la Rosa).

many different nondestructive-evaluation (NDE) methods that have been tested or used with this purpose [12–14]. The most common techniques are ultrasonic inspection, x-ray tomography, thermography, and microwave imaging. Terahertz (THz) pulsed imaging is a promising alternative that provides several attractive features but presents challenges. It has appropriate spatial resolution (due to its wavelength, $\lambda \sim$ 300 μm in the air at 1 THz) to identify critical structural characteristics and defects. Moreover, since THz electromagnetic radiation penetrates polymers and glass, quantitative structural information at depth can potentially be obtained. In addition, THz radiation is nonionizing, as opposed to x-rays, and thus presents minimal health risks to the operator. Compared to standard approaches such as ultrasonic imaging, THz waves require no coupling fluid, and the materials are relatively transmitting, unlike ultrasonic signals at the high frequencies required to obtain quantitative three-dimensional information at depth.

THz-based techniques have already drawn attention in the last decade for the NDE of GFRP materials. Continuous-wave (CW) THz systems, which work with monochromatic electromagnetic radiation, have already provided interesting results on the damage detection and inspection of various polymeric and composite materials [15–17], though usually not providing depth information. Several studies [2,3, 18–20] have also successfully used pulsed THz radiation to observe the presence of buried defects in GFRP laminates. For instance, Jördens and co-workers [21] used THz time-domain spectroscopy (THz-TDS) to explore the birefringent properties of unidirectionally oriented GFRP. They showed how the refractive index and absorption coefficient depend on the relative orientation between the THz polarization and the glass fibers. Similar procedures have been later applied by other authors [22]. In a recent paper [23], Park et al. used the same birefringence principle to predict the primary fibers' orientation and differentiate between three different stacking sequences of woven fibers. This THz-TDS approach leveraging off the fabric-induced birefringence has hitherto been restricted to determining the fibers' orientation, and not used to extract more detailed information concerning the woven fabrics. With a somewhat different type of material, Tang et al. [24] measured the orientation and spacing between fibers in a silk-nylon woven sample based on Fraunhofer diffraction. Similar research has been conducted on CFRP, where defects and damage have been observed [19,25–27]. However, the THz wave penetration was limited because of the conductivity of the carbon fibers; hence hindering analyses in-depth.

In this work, we observe woven fabrics and quantify their process-induced microstructure in three dimensions in GFRP laminates. Our approach is based on a THz raster scan in reflection by a concatenation of image and signal processing tools to extract specific information about the weave structure, such as the fiber orientation and the gap between two tows, in the various plies. Specifically, the approach provides a quantitative and global measure of the orientation of tows within the weave pattern and their period. These quantities are characterizable and can ascertain the origin of the material's manufacturing or its damage in service. The proposed approach could be easily implemented in standard C-scan inspection.

2. Materials and methods

2.1. Sample

The studied material is a woven twill 2/2 composite called Vizilon SB63G1-T1.5-S3, manufactured by DuPont de Nemours using a thermo-compression molding process. It is a co-polyamide 6.6/6 (PA 6.6/6, thermoplastic matrix) reinforced with a layup of three balanced glass fiber plies oriented at $\pm$ 45° (warp and weft yarns) as shown in Fig. 1. The composite, with a thickness of 1.53 mm, has a fiber weight ratio of 63%, corresponding to a fiber volume fraction of 43%. The sample has a surface dimension of 21 mm $\times$ 77 mm. A detailed structural characterization of the same material can be found in Ref. [28].

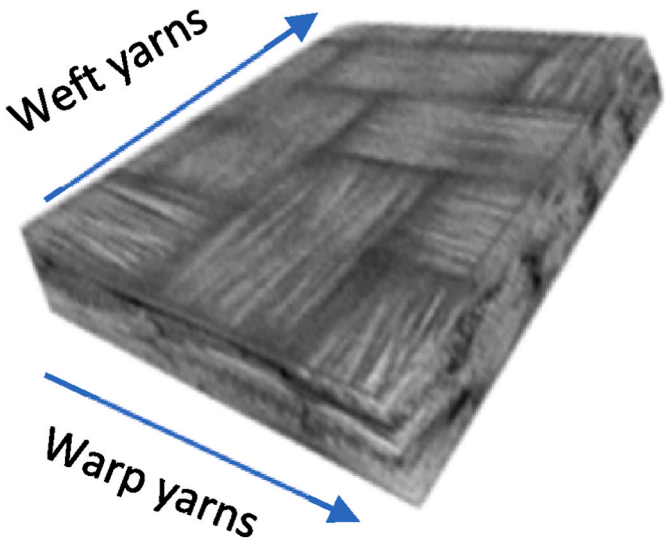

Fig. 1. Reinforcement architecture of the woven glass fabric-PA 6.6/6 composite showing the warp and weft yarns [13].

2.2. Experiment

We conduct THz imaging of the composite sample with a TPS Spectra 3000 (TeraView, Cambridge, UK) in reflection mode at room temperature (25 °C). The full sample surface was raster scanned with roughly single-cycle THz pulses with a transverse spatial step size of 0.4 mm for both the *x* and *y* directions (parallel to the sample's surface), leading to $\sim$ 53 $\times$ 193 pixel images. These pulses impinge on the sample near-normal incidence, and the reflected signal is detected close to the specular direction. Due to refractive-index discontinuities, reflected pulses (*echoes*) occur. The time delay at their detection allows the construction of the sample's depth profile at the position studied if we know the refractive indices. Repeating this process for all pixels, we can obtain a three-dimensional dataset representative of the sample structure. Finally, we produce a two-dimensional cut of this dataset, showing the reflected intensity at each pixel for a given time delay, which is commonly known as a C-scan.

The spatial resolution of the measurement has two components. The first one is the *transverse resolution*, which is close to the spatial step size (in our experiments, the step size is slightly larger than the beam spot size - about ~300 μm at 1 THz-on the surface). The second one is the *axial resolution*, which is linked to half the shortest wavelength present in the high signal-to-noise band within the medium, which in our case is ~46 μm.

2.3. Image-processing algorithm

In this subsection, we present our THz imaging workflow and methodology. It relies on the Fourier analysis of raw THz images (C-scans) and the searching of spectral signature (and their associated characteristics) of periodic structures. The results obtained at each step will be presented later - in *Section 3.1* - in the same order in which they have been applied. All the image processing has been implemented in Python® and its libraries. Fig. 2 is a schematic representation of the various methods applied, from the raw THz image to the extraction of the desired parameters.

The first step is *image averaging*. In this process, we produce a new low-pass filtered C-scan where the intensity of each pixel is the average of $(2n+1)^2$ neighboring pixels (*n* pixels in each direction) in the raw image. The aim is to smoothen the image by reducing high-spatial-frequency noise. For a number *n* of neighbors, the averaged intensity $\bar{I}_{i,j}$ of a pixel with spatial coordinates (i,j) is

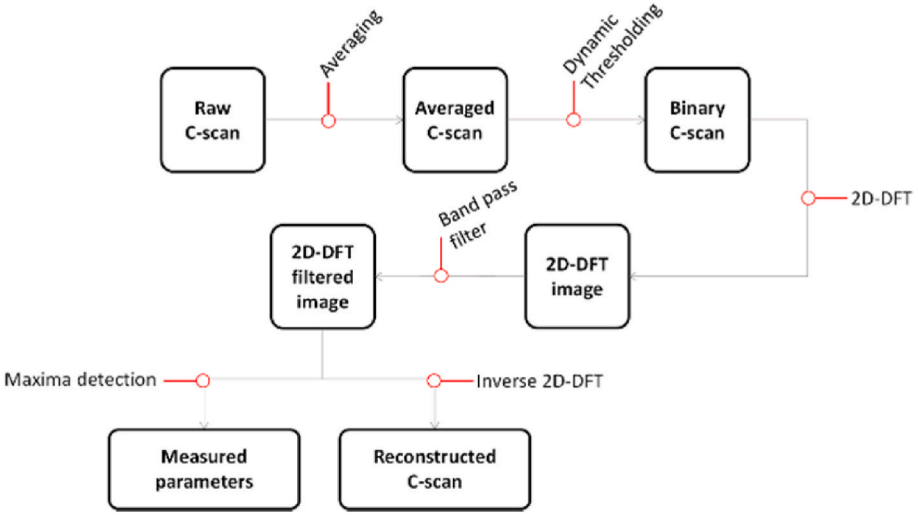

Fig. 2. Schematic description of the methodology followed by the developed image processing algorithm.

$$\bar{I}_{i,j} = \frac{\sum_{y=j-n}^{j+n} \sum_{x=i-n}^{i+n} I_{x,y}}{(2n+1)^2} \tag{1}$$

where $I_{x,y}$ represents the measured intensity at pixel (x,y). We correct for those pixels where i or $j < n$ (*i.e.,* at the edge of the image).

The second step is binarization [29,30], which helps distinguish between different materials or objects in the image. We have used a global thresholding method in situations where the distinction between the two materials is evident. As a result, pixels with an intensity larger than a defined threshold T are set to one and zero otherwise. In more complicated situations (such as in fibers-matrix differentiation), the adaptive (also called dynamic) thresholding approach has been used [31]. In this case, the local threshold value $T_{i,j}$ is the weighted mean of the neighbors of pixel (i,j). The number of neighbors considered in each direction (*i.e.*, the threshold *radius*) has been set to 3. Thus, in both binarization methods, each pixel has a final binary value $B_{i,j}$ obtained by applying the criterion

$$B_{i,j} = \begin{cases} 1 \text{ if } \bar{I}_{i,j} > T_{i,j} \\ 0 \text{ otherwise} \end{cases} \tag{2}$$

The third step relies on computing the two-dimensional discrete Fourier transform (2D-DFT), a commonly-used processing tool for filtering images and extracting features of interest [29,32]. Here, we aim at extracting characteristics of periodic patterns (*i.e.*, the weave structure in the composite); the 2D-DFT should exhibit pronounced peaks at spatial frequencies corresponding to these periodicities [33]. The 2D-DFT is given by

$$X(u,v) = \sum_{m=0}^{M-1} \sum_{n=0}^{N-1} x(m,n) e^{-j2\pi\left(\frac{um}{M}+\frac{vn}{N}\right)} \tag{3}$$

where $x(m,n)$ is the intensity of pixel (m,n) in the spatial domain in a M x N-pixel image, $X(u,v)$ is the complex-valued magnitude at the (u,v) coordinates in the 2D spectral domain, and $j = \sqrt{-1}$. The radial (spatial) frequency u_r is defined as $u_r = \sqrt{u^2+v^2}$, and the angle with respect the horizontal zero frequency axis θ as $\theta = \tan^{-1}(v/u)$ [33]. In case that $u = 0$, $\theta = 90°$ if $v > 0$ and $\theta = -90°$ if $v < 0$.

Finally, in the fourth and final step, we implement a high-pass filter [29,30] to remove low-level spatial frequency noise in the obtained 2D spectra. As we apply this filter in just one of the directions (u or v) at each step, we set a wavenumber threshold ($wT_{u/v}$) below which all the intensities are set to zero for this specific direction. The criterion is

$$F_{u,v} = \begin{cases} X_{u,v} if\ u/v > wT_{u/v} \\ 0 \text{otherwise} \end{cases} \tag{4}$$

where $F_{u,v}$ is thus the filtered complex-valued magnitude at (u,v) coordinate in the spectral domain.

To summarize, in steps 1 and 2, the original spatial-domain image is adapted to reveal the matrix-fiber microstructure for a given time slice. Once both phases are differentiated, we proceed in step 3 to apply a 2D-DFT to obtain well-defined peaks in the spectral domain, associated with the mean woven structure. In step 4, filtering of the 2DFTT separates the periodic structure from the noise. The resulting 2D spectrum has two purposes: (i) Locate the maxima and calculate the corresponding distance and angle in the spatial-domain, and (ii) perform the inverse 2D-DFT and obtain a graphical representation of the mean fibers' arrangement in the sample. We have repeated this methodology with multiple C-scans obtained at different time delays to ensure the robustness of our analysis.

It is worthy of note that, in addition to the image processing techniques described here, signal processing of the temporal signal corresponding to each pixel is also applied, as described later, to account for the noise of the experimental THz pulse. Specific parameter values used in the various image and signal processing steps might need to be adapted to the sample under investigation, though, in the following, we guide the reader by discussing how these parameter values are determined.

3. Results and discussion

The measurement and the subsequent data analysis correspond to a basic THz time-of-flight tomography (TOFT) experiment [34,35]. Depth information in THz TOFT is extracted from echoes in the reflected signal at a given spatial location, which originates from a discontinuity in the refractive index (such as those induced by the matrix-fiber-bundle interface). The depth information is in the relative time delays between the various echoes (accounting for the refractive indices of the materials). The process is then repeated at all transverse pixels across the sample area, leading to a block of three-dimensional data (two spatial dimensions x and y, one temporal dimension).

One way to represent this information is to take a 2D cut through the data (using one spatial dimension and the time dimension) to produce a B-scan, which provides a cross section through the sample, time serving as a surrogate for the axial coordinate. Fig. 3 shows the B-scan obtained at approximately the center of the sample along the short axis ($y = 30$ mm). To increase the contrast and facilitate the observation of the

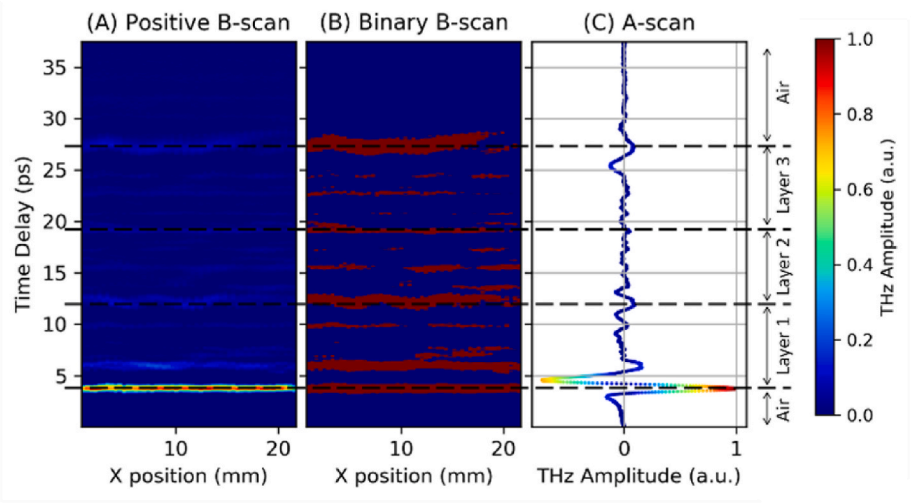

Fig. 3. B-scan obtained for a cross-section along the short axis ($y = 30$ mm) at the center of the sample. (A) Negative amplitudes have been set to zero in order to increase the contrast. (B) Binary B-scan obtained with a global threshold of 2.5% of the maximum intensity. (C) THz pulse amplitude in time (A-scan) is located at $y = 30$ mm and $x = 10$ mm. The THz signal impinges from below (small time delays), and the horizontal dashed lines locate the interfaces found in the sample.

various echoes at the interfaces, we plot only the positive amplitudes in Fig. 3 (A). Fig. 3 (B) represents binary B-scan for a global threshold of 2.5% of the maximum intensity, showing each of the interfaces (i.e., surfaces between two consecutive layers) separated by a constant time delay of 8 ps (at around 4, 12, 20 and 28 ps). Due to the physical discontinuity, there is a change in the refractive index and a more significant reflection at these points. The structure deduced matches the peaks found at each THz pulse [*i.e.*, in an A-scan, Fig. 3 (C)]. We also observe additional reflections in the intermediate regions originating from the different reflectivity between the glass fibers and the polymeric matrix.

The air-sample interface stands out at 4 ps in Fig. 3 as a pronounced red band due to the large refractive-index mismatch between air and the polymer matrix. One observes successive maxima at increasing time delays within the sample, showing a tendency to form horizontal bands in the B-scan. These red bands correspond to abrupt changes in refractive index, as it may happen for interfaces such as air-polymer, polymer-glass fibers or inter-ply interfaces. That is, echoes occur due to the stratified nature of the CFRP laminate. Due to the different refractive indices of the matrix and glass-fiber bundles, these bands reveal the woven structure at various depths. However, it is challenging to directly extract clear quantitative information on the material internal structure from this three-dimensional dataset.

To better extract quantitative information about the weave structure, it is more fruitful to consider C-scans, *i.e.,* two-dimensional sections parallel to the surface within a narrow time-delay window. Below, in Sec. 3.1, we first present a complete analysis from the main echo (air-sample interface) study, revealing the characteristics of the fabric in the first layer. Section 3.2 shows how the proposed algorithm can examine the fabric in the three deeper layers. Finally, in Sec. 3.3 the accuracy of the method is confirmed by using a larger set of artificially created noisy C-scans.

3.1. First echo analysis

The measured THz pulses have been initially processed using typical denoising procedures to overcome experimental artifacts. In our case, we first applied an ideal high-pass filter with a cutoff frequency of 0.2 THz (which removes low-frequency noise) and the resulting pulse was filtered with frequency-wavelet domain deconvolution to reduce noise [36,37]. Fig. 4 shows an averaged (see above) C-scan at the sample's surface (time delay ~4 ps) obtained from these pulses. The optimal number of neighbors used in the averaging is determined to be 2 for these samples; this value helps remove image noise while not introducing significant blur that would complicate the distinction of the bundles.

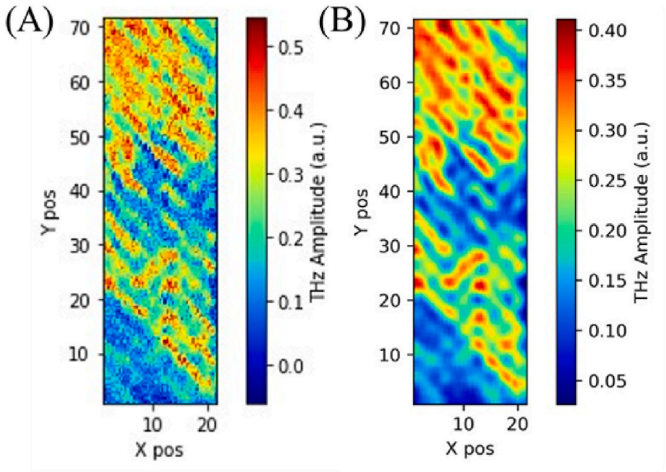

Fig. 4. (A) Raw and (B) averaged with $n = 2$ neighbors C-scans at the sample surface (4 ps). The two perpendicular fiber bundles (at $\pm 45°$) are clearly visible.

This image reveals the presence of two perpendicular fiber bundles oriented at $\pm 45°$ (warp and weft), in good agreement with the manufacturer's description. We observe a magnified amplitude of the reflected signal at the center of each bundle. It results from the enhanced reflection of the THz pulse at this position under normal incidence at the top of their circular cross-section. Subsequently, we binarize this C-scan to identify the fibers better and differentiate them from the matrix. To do so, we have used an adaptive thresholding method, as illustrated in Fig. 5 (A). The definition of the borders between the fibers and the matrix is not well resolved. Assuming a continuous shape of the fibers, we have smoothened the binary C-scan with an image-averaging procedure. The result is shown in Fig. 5 (B).

The improvement in the definition of the fibers is substantial. Indeed, Fig. 5 (B) provides clear identification of the matrix (blue) and fibers (red).

Once the two materials are well-differentiated, we take the 2D-DFT of the image to quantify the periodicities present. The modulus square

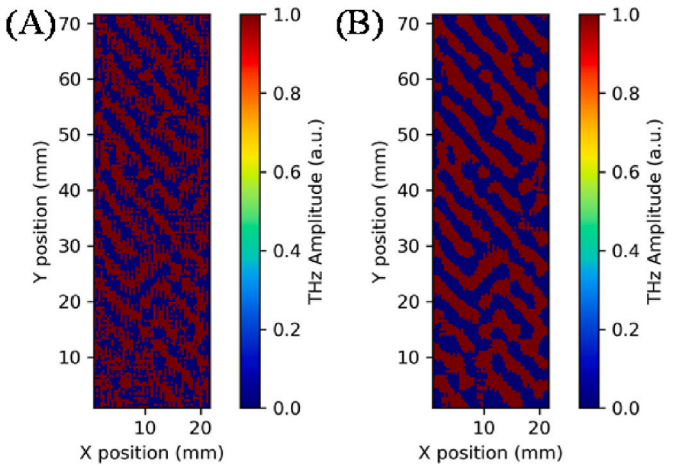

Fig. 5. (A) Binary C-scan obtained with an adaptive thresholding with 3 neighbors, and (B) smoothed binary C-scan obtained after averaging with $n = 2$ and thresholding at 50% of the intensity to increase the fibers' definition. The matrix part is in blue, and the reinforcement tows are in red in each picture. (For interpretation of the references to colour in this figure legend, the reader is referred to the Web version of this article.)

of the 2D-DFT of Fig. 5 (B) is shown in Fig. 6 (A).

The image exhibits four peaks surrounding the zero-frequency point (itself of no interest) in the two directions of the periodicities seen in the C-scans. Two peaks (corresponding to one of the two bundles' orientations) are stronger than the other two due to the more pronounced appearance of one of the directions in the C-scan (Fig. 4). This difference in magnitude of the two fiber orientations is attributed to birefringence. It is essential to highlight that the quality of the experimental measurements influences the contrast in this analysis. The peaks have a nonzero spectral extent due to (i) the finite sample size (much smaller in the horizontal than vertical directions, given greater horizontal extension of the sample) and (ii) departures from the ideal periodicity of the fiber bundles.

To optimize the extraction of information from the four prominent peaks, we have first applied a combination of a horizontal and a vertical high-pass filter to eliminate all these noisy periodic signals along the vertical and horizontal axes. By this process, we set all pixels' intensity to zero when they are below a defined wavenumber threshold for each axis. In this case, we have used a 4×10^{-2} mm^{-1} threshold for both cases, considering the extension in the spatial frequency domain of the central noise in Fig. 6 (A). The result is shown in Fig. 6 (B).

The horizontal and vertical noisy patterns have been eliminated - as well as the central peak. Consequently, the four peaks representing the constant texture in the C-scans can be better differentiated, especially the two weaker ones. The downside of this process is the detection of lower-intensity parasitic signals in the background, which do not represent the main fibers' pattern. Nevertheless, given that the relative intensity of the noise is lower than that of the peaks, it can be eliminated by a simple thresholding process. Due to the difference in relative intensity between the two pairs of peaks, we define a threshold at 80% of the maximum intensity for each of the directions (*i.e.*, at each of the four 2D-DFT quadrants) to ensure correct detection. Smaller threshold values might introduce background noise, while larger ones could lead to the loss of meaningful peaks. The result is shown in Fig. 6 (C), in which the centers of the peaks can be clearly identified. The spectral coordinates are $u = -0.19$ mm^{-1} and $v = 0.17$ mm^{-1} for the upper-left peak (the weakest, corresponding to the *warp* direction), while the coordinates are $u = 0.18$ mm^{-1} and $v = 0.17$ mm^{-1} for the upper-right peak (the most intense, associated to the *weft* direction). Due to the symmetric nature of the 2D-DFT we only consider the peaks in the upper half of the image. These coordinates are used to calculate the corresponding radial frequency and angle in the frequency domain, which result in $u_r = 0.26$ mm^{-1} and $\theta = -41.61°$ for the left-side peak, and $u_r = 0.25$ mm^{-1} and $\theta = 44.52°$ for the right-side peak. The corresponding space-domain distance is 3.86 mm for the warp direction and 4.05 mm for the weft direction. This distance corresponds to the distance between the ridges observed in the C-scans, *i.e.,* the average distance between the top of the fiber bundles. Additionally, the quantitative measurement of the fiber orientations leads to the respective values of 41.61° and −44.52° with respect to the vertical axis (see Fig. 7 (C) for a schematic representation). We notice that the weave pattern does not form a perfect right angle. Therefore, with this method, we can also detect assembly irregularities between the different bundles. Overall, the values are in good agreement with the theoretical values provided by the manufacturer, the structural data given in Ref. [28], and the C-scan shown in Fig. 4.

To check the accuracy of our results, we have tested this algorithm with the surface C-scans of a set of four different samples made of the same material. We have obtained a mean distance value of 3.90 ± 0.03 mm, an orientation of $42.90 \pm 1.82°$ for the warp direction, a mean distance value of 4.08 ± 0.08 mm, and an orientation of $-45.63 \pm 0.92°$ for the weft. It reflects the consistency of the extracted data.

Finally, we have used the processed 2D-DFT image, represented in Fig. 6 (C), to perform the inverse 2D-DFT and obtain a clear representation of the mean disposition of the fibers at this specific time delay. In order to allow easy comparison, we provide in Fig. 7 (A) the obtained inverse 2D-DFT together with the averaged C-scan in Fig. 7 (B).

After the image processing, we see that Fig. 7 (A) reveals the fiber structure suggested by the C-scan. As expected from the experimental C-scan, one of the two diagonals (weft) is more intense than the other (warp). In addition, the positions with higher intensity result from the intersection of the two diagonal patterns, leading to a stronger intensity in these points.

In conclusion, the proposed method does not only allow one to extract quantitative information about the woven fabrics, but it also

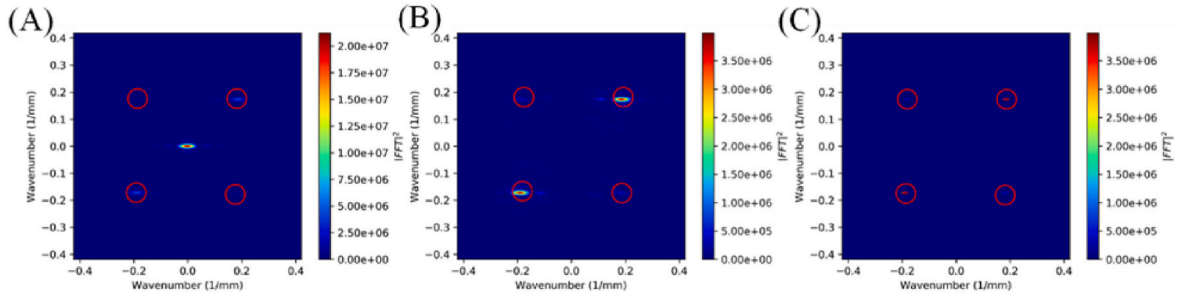

Fig. 6. (A) Modulus square of the 2D-DFT of the image in Fig. 4 (B), (B) 2D-DFT modulus squared image using a wavenumber threshold of 4×10^{-2} mm^{-1} on the horizontal and vertical axis, (C) 2D-DFT modulus squared image after an 80% of maximum intensity threshold. Four prominent peaks (circled in red) are visible which give the directions of the periodicities in the C-scans. (For interpretation of the references to colour in this figure legend, the reader is referred to the Web version of this article.)

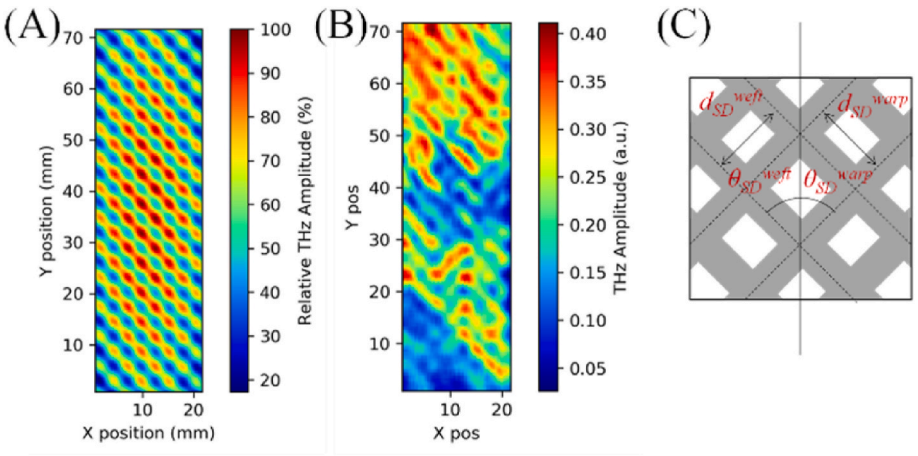

Fig. 7. Comparison between (A) inverse 2DFFT representing the mean fibers' structure after processing the image, and (B) experimental averaged C-scan, both at 4 ps. (C) graphically shows the space-domain distance (d_{SD}) and angle (θ_{SD}) criteria used in the calculation. Similar to the experimental C-scan, one orientation is more intense than the other in the inverse 2DFFT.

leads to a clear and faithful representation of the fibers. In the next section, we exploit the same procedure to C-scans obtained at different time delays, leading to the extraction of in-depth (and thus, three-dimensional) sample information.

3.2. *In-depth analysis*

We analyze here multiple C-scans, obtained at various time delays, to extract information about the weave structure in subsurface plies of one laminate. To do so, we select the optical delays corresponding to the three interfaces previously identified (12.0, 19.5, and 27.5 ps), and an inner point of the first layer that has a strong reflection (6.0 ps). In Fig. 8, we present the B-scan with the selected time delays marked and corresponding C-scans.

From Fig. 8, we observe that there is still a preferential fiber-bundle direction, as on the surface, although both may be observed in all cases. On the other hand, the weave patterns appear to be less clear than in the surface-ply C-scan, and it can even be difficult to identify them visually from the raw C-scans. It is the consequence of the increased signal attenuation at larger depths, which leads to an increased role of noise. Moreover, as one concentrates on longer time delays, shadow effects due to overlying features contribute artifacts to the C-scans. However, the contrast and quality of the C-scan increases again for the back surface of the sample (27.5 ps). It is due to a larger refractive index mismatch between the sample and air. We have applied the same algorithm, with the same parameters as in Section 3.2, to reveal the woven structure and extract quantitative information. The summarized results are presented in Fig. 9.

The background noise is, in all cases, slightly larger than in the 2D-DFT pattern obtained for the C-scan at 4 ps due to the lower signal to noise associated with subsurface plies. Again, the 2D high-pass filter of the 2D-DFT allows us to remove the main peak and noise and thus

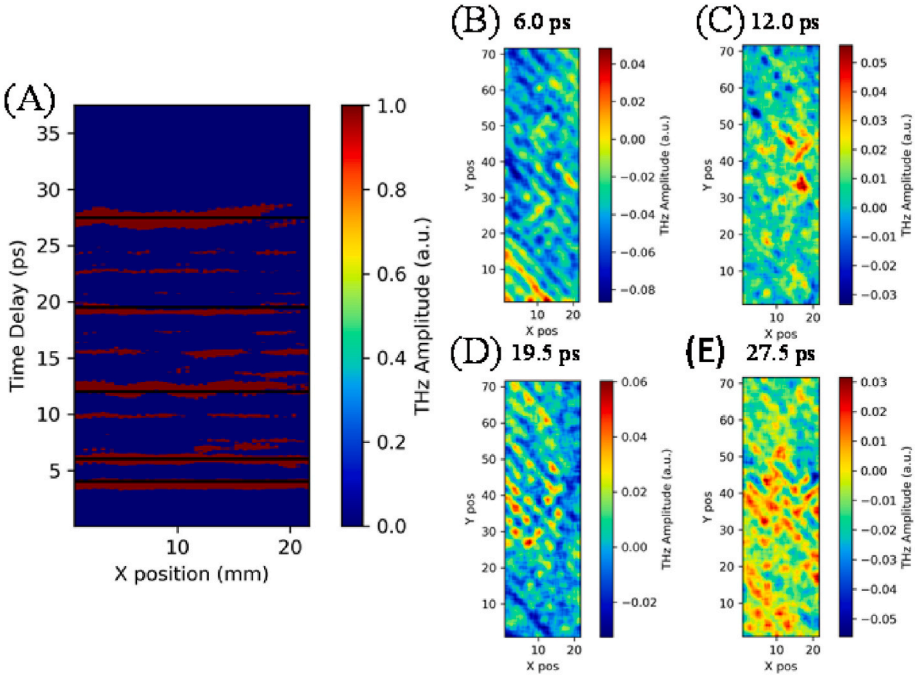

Fig. 8. (A) Binary B-scan with different selected time delays marked with dark lines, and its corresponding averaged C-scans at (B) 6.0 ps, (C) 12.0 ps, (D) 19.5 ps, and (E) 27.5 ps. The ±45° weave pattern is still visible in the C-scans in depth.

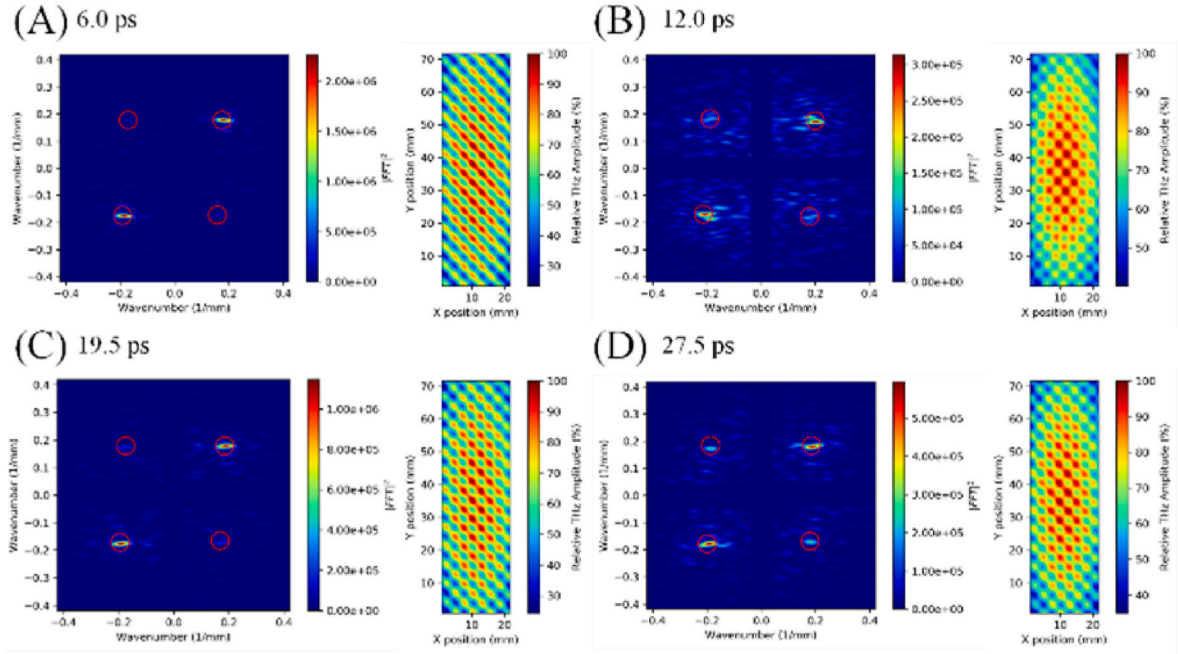

Fig. 9. Filtered modulus square 2D-DFT patterns and inverse-2D-DFT sample reconstructions obtained from the averaged C-scans at (A) 6.0 ps, (B) 12.0 ps, (C) 19.5 ps, and (D) 27.5 ps. Similar to what is presented in Fig. 6, the 2D-DFT patterns have been threshold at 80% of the maximum intensity after a filtering consisting of a 4 $\times$ 10^{-2} mm^{-1} cutoff wavenumber on the horizontal and vertical axes. The main peaks are circled in red. (For interpretation of the references to colour in this figure legend, the reader is referred to the Web version of this article.)

identify the peaks corresponding to the woven structure. These filtered squared modulus 2D-DFT images have been thresholded at 80% of the maximum intensity in each direction, and the inverse 2D-DFT has been computed to reconstruct the woven fabrics. As the reader may notice, despite the lower definition of the raw C-scans, this process can identify the fiber-bundle directions and reveal the fabric structure. Compared with the surface analysis, these results are of importance due to two aspects: first, we observe the woven fabric deeper than the surface ply thanks to the penetration of THz waves. Second, the proposed image and signal processing enhances the physical measurement and reveals the periodic fabrics from C-scans, where this information is not apparent to the eye in the raw C-scans.

Finally, by computing the coordinates of the modulus squared 2D-DFT, we deduce the fibers' orientation and spacing at different depths (see Table 1). The standard deviation for the orientations of the bundles over all the plies is 1.30° and 1.48°, respectively. It is in the expected order of magnitude, when compared with other studies dealing with fiber orientations dispersion through the thickness on similar materials [38,39]. The consistency of these values—and their agreement with the manufacturer's values—demonstrates that the woven fabrics are the same and have similar orientations in each layer, which is reasonable as the sample has been analyzed as received, without suffering deformation or damage. At the same time, this becomes a powerful tool to measure and control small deviations from the ideal values expected from design at each ply and depth.

Table 1
Numerical results of the measurement of the fiber bundles' orientation and distance at each ply. No significant variation of the orientations and spacing of the fibers is noticed over the layers. The "*interface*" column indicates between which two layers the time delay is placed. The round brackets indicate that the position corresponds to an inner point of a layer.

Interface (prev.-next)	Time delay (ps)	Weft direction		Warp direction	
		θ_{SD} (°)	d_{SD} (mm)	θ_{SD} (°)	d_{SD} (mm)
Air-1	4.0	−44.52	4.05	41.61	3.86
(1)	6.0	−47.14	4.17	42.89	3.87
1–2	12.0	−44.86	3.93	38.97	3.86
2–3	19.5	−45.23	4.10	41.82	3.76
3-Air	27.5	−43.61	4.01	42.02	3.75
Mean		−45.07	4.05	41.46	3.79
STD		1.30	0.09	1.48	0.08

3.3. *Method accuracy – simulation analysis*

After having proven that the approach works with real samples, we test its accuracy and robustness. To do so, we work with artificially produced C-scans, because we can generate a wider range of sample characteristics and, at the same time, we remove all the experimental error, limitations, or noise.

With this goal, using a Python® code, we have generated a set of binary C-scans with the two fiber-bundle directions (mimicking the sample studied in this work) but varying the two measurable parameters and creating all their possible combinations: (i) orientations from the 10° to the 80° from the vertical axis, in steps of 5°; (ii) distances from 2 mm to 6 mm, in steps of 0.5 mm. We have therefore tested 135 different binary C-scans. The fibers' width is set to 1 mm, the sample size to 60 mm in the *y*-direction and 20 mm in the *x*-direction, and a pixel step size of 0.25 mm in both directions. To provide a general view of the patterns created, Fig. 10 shows the four most extreme cases.

From Fig. 10 it can be noticed how the 2D-DFT peak distribution changes according to the fibers' orientations and distance in the C-scans. Obviously, contrary to the experimental sample, there is no background noise due to the almost perfectly defined texture in the simulated C-scans. These 2D-DFTs have been filtered and thresholded, as we previously did with the experimental sample. Then, the coordinates of the peaks defining the weave fabrics have been determined to calculate their corresponding distance and angle in the space domain. For all the 135 combinations, the obtained results are plotted in Fig. 11 (A) for the measured distances and Fig. 11 (B) for the measured angles. To analyze the accuracy of the measurement, we have compared each measured value with the real one to calculate the relative error (ε_r) as

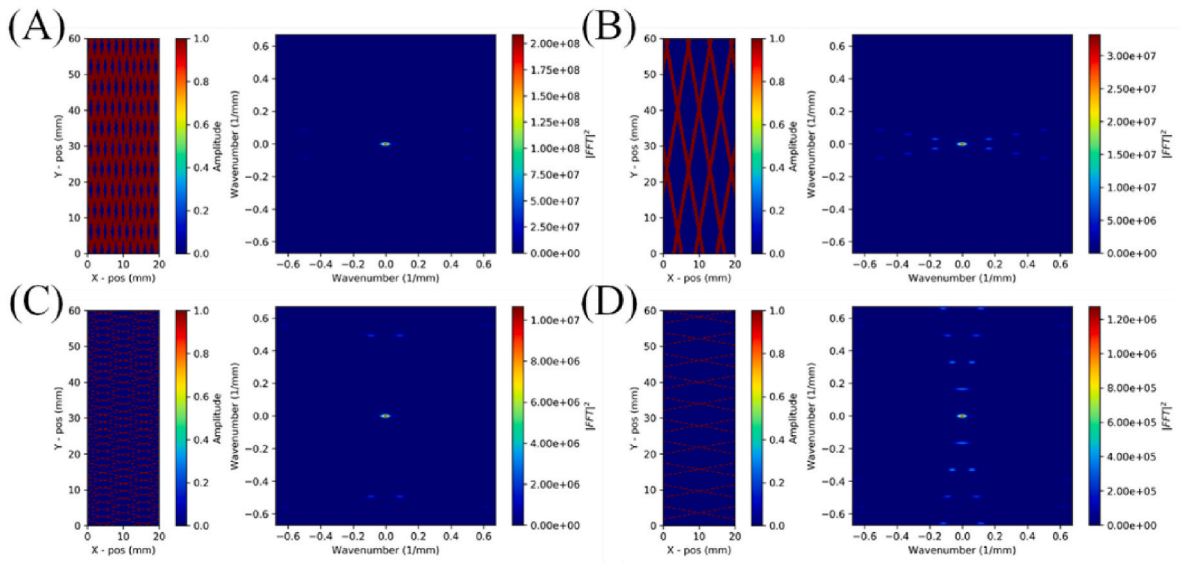

Fig. 10. Simulated binary C-scans and their corresponding modulus squared 2DFFT images for the conditions: (A) 10° and 2 mm, (B) 10° and 6 mm, (C) 80° and 2 mm, and (D) 80° and 6 mm. The matrix is in blue and the fibers in red in the simulated C-scans. The four main peaks are circled in red. (For interpretation of the references to colour in this figure legend, the reader is referred to the Web version of this article.)

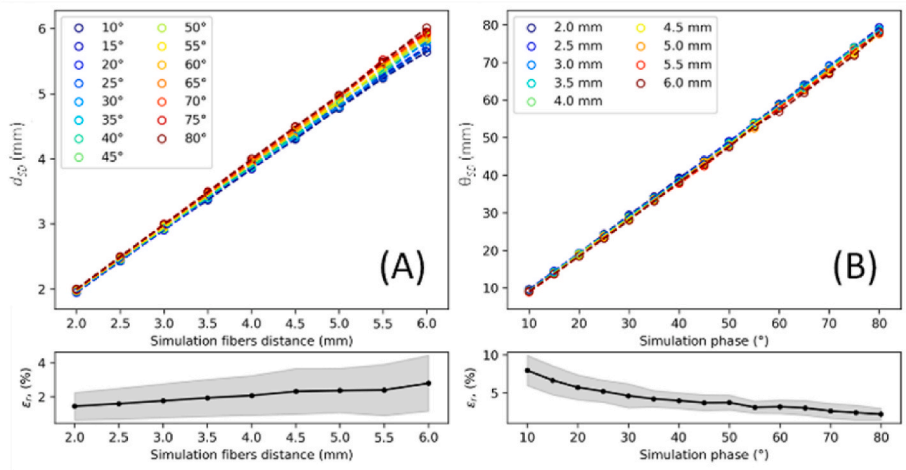

Fig. 11. (A) Measured distance vs simulation (real) distance, and (B) Measured angle vs simulation (real) angle. The corresponding mean and standard deviation values for the relative error are represented at the bottom of the figure. A high degree of agreement between the simulated and measured values is observed.

$$\varepsilon_r = 100\ \frac{|X^R - X^C|}{|X^R|} \tag{5}$$

where X^R and X^C refer, respectively, to the real and calculated values of the magnitude X, which can be either the distance or angle. These errors have been estimated, as a function of the simulation distance and simulation angle and are presented in the bottom part of Fig. 11.

The top plots in Fig. 11 show that the measured values (y-axis) are almost identical to those used to simulate the C-scan (x-axis), independently of the other magnitude value. This excellent agreement between both values confirms the performance of our method, leading to accurate quantitative data of the former structure. In addition, the accuracy has been quantitatively calculated by computing the relative error. In terms of the distance measurement, the obtained errors range from 1.4% to 2.8%, confirming the precision of the method. In addition, in the bottom plot of Fig. 11 (A), it can be observed how the relative error slightly increases as the distance between fibers increases (*i.e.*, this approach is more accurate for closely packed weave fabrics). This change in the accuracy might be produced because the distance between the 2D-DFT peaks decreases when the distance in the space domain increases, and thus the peaks start to overlap and become more difficult to differentiate.

On the other hand, the relative error on the angle measurements ranges from 2.1% to 7.9%. In this case, the accuracy is better for high-angle (*i.e.*, almost horizontal) fibers orientation. It is the result of the error propagation in the angle calculation in the frequency domain [$\theta = \tan^{-1}(v/u)$]. The smaller the fibers' angle (i.e. the more vertical the orientation), the shorter the v/u ratio in the frequency domain. Therefore, a small error in the coordinates' approximation leads to a proportionally larger relative error when computing the ratio v/u. However, the larger the fibers' angular orientation, the larger the v/u ratio and, thus, the smaller the relative error despite having the same absolute error in the determination of the coordinates (u, v). In this regard, one can check that - contrary to Fig. 11 (A) - in Fig. 11 (B) the absolute error (or dispersion of results) is almost constant in all the angular range, and therefore the difference comes from the relative calculation discussed above.

These results confirm the intrinsic good performance of our

algorithm when the experimental conditions do not add significant noise to the raw image. However, as it has been proved in *Section 3.2*, this procedure has the potential to reveal structures that are difficult to identify by eye. With this in mind, we have tested our approach with a batch of artificial C-scans with added noise and blurring effects, in order to replicate real C-scans with different grades of experimental noise. To do so, we have produced binary C-scans with $\theta_{SD} = 45^{\circ}$ and $d_{SD} = 4$ mm (the same as the real samples examined before) and added different types of noise and blurring: (i) First, we have added Gaussian noise by replacing random pixels with intensities within a gaussian distribution centered at 0.5 (the average intensity in the binary C-scans). The standard deviation (*SD* or σ) of the Gaussian distribution has been varied to see how the dispersion of intensities affects the quality of the measurements; (ii) Another strategy has been to add salt and pepper (*S&P*) noise, where different amounts of binary pixels (white and black, or 0 and 1) are randomly distributed through the image. The ratio between *salt* and *pepper* pixels has been kept constant (1:1) while the effect of the number of substituted pixels has been analyzed; (iii) Finally, we have also tested the effect of blurring effects in the image by using a Gaussian kernel with different *SD* and a constant truncation of 3.

Fig. 12 shows the most extreme cases that we have produced by each approach. Each column corresponds to one of the methods (Gaussian noise, *S&P* noise, and Gaussian blurring, respectively); the top images show the weaker noise cases and in the bottom are represented the cases with the most significant alterations. In total, we have tested 21 noise values for each case to evaluate the accuracy of our approach. The results are depicted in Fig. 13. Furthermore, given that the two first approaches have a random component, we have performed 10 replicates with the aim of obtaining more statistically meaningful data.

Concerning the Gaussian-type noise, we may first observe the high degree of perturbation reached in our simulations. However, we must notice that the accuracy is excellent while $\sigma < 2$. In this range, the error in the distance measurement is stable around 1.5%, while it oscillates between a 2 and 3% in the case of the angular measurement. Both are very low values and are in excellent agreement with the results shown before in Fig. 11 where the C-scans did not contain any noise. Therefore, we can conclude that the measurement is not affected by the noise until these levels. For $\sigma \geq 2$ the error in the angular measurement remains stable, but it starts to oscillate for the distance. For the case $\sigma = 2.42$ (where the error reaches a maximum), the distances measured for the 10 replicates are respectively 3.92, 3.94, 25.84, 3.92, 3.92, 3.99, 3.99, 3.92 and 3.99 mm. 9 out of the 10 cases are close to the simulation value of 4

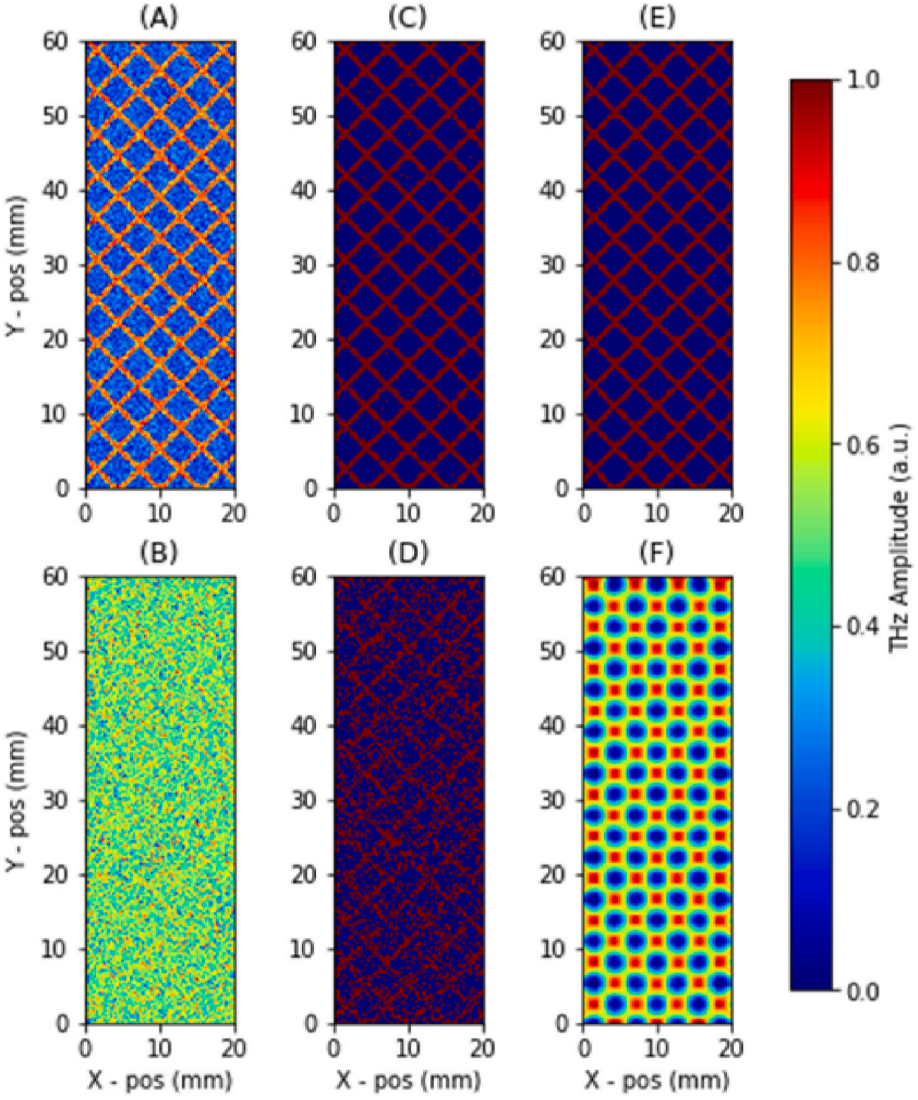

Fig. 12. Simulated C-scans with added noise and blurring effects. First column (A and B) corresponds to Gaussian noise with $\sigma = 0.1$ and $\sigma = 3.0$ respectively; Second column (C and D) corresponds to S&P noise with a 1% and 75% of the image pixels substituted; Third column (E and F) corresponds to C-scans blurred by using $\sigma = 0.1$ and $\sigma = 3.0$, respectively.

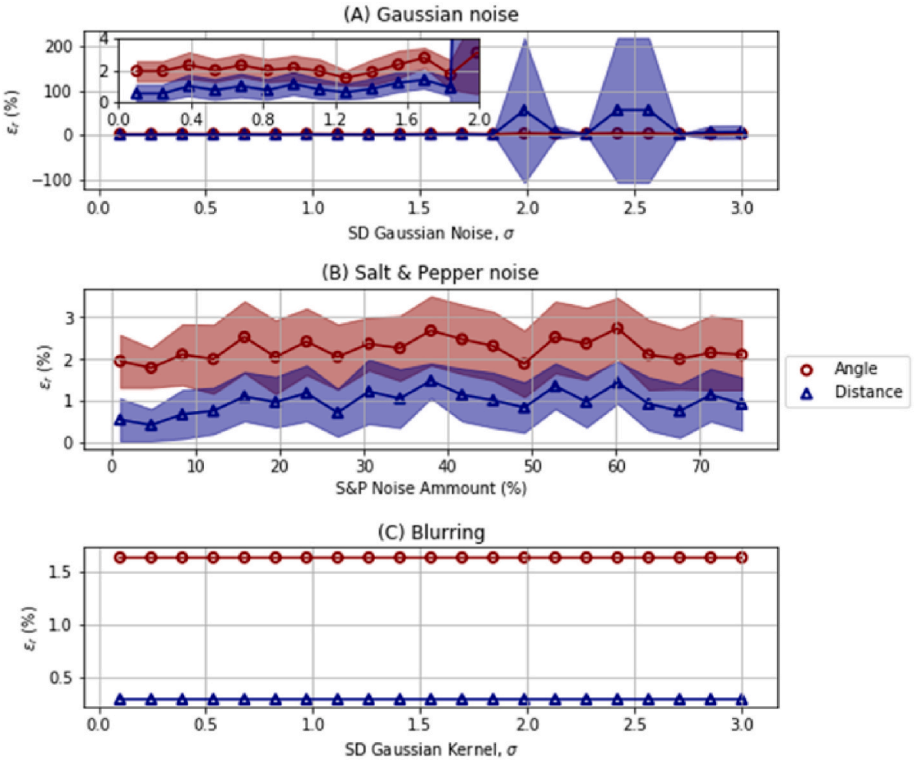

Fig. 13. Accuracy of the proposed method for different types and levels of noise. (A) Shows the mean and standard deviation (shadowed region) values of the relative error of the measurement when Gaussian noise is added to the C-scan. The inner plot zooms into the region where $0<\sigma<2$ to facilitate its visualization; (B) Shows the mean and standard deviation (shadowed region) values of the relative error of the measurement when *S&P* noise is added to the C-scan; (C) Shows the relative error of the measurement when the C-scan is blurred by using a Gaussian kernel.

mm, but there is one result at 25.84 mm which is responsible for the huge increase in the relative error. Given that there is almost no error in the angular measurement, the algorithm is measuring a pattern with a larger period in the same direction, but not having a significant error in the pattern measurement. Thus, for large values of noise there is a higher probability to hide the fiber bundles and make other less frequent periodicities more visible. However, we must highlight that the method is still working in most cases (90%) with high accuracy, while visual inspection is almost impossible.

In the *S&P* case [Fig. 13 (B)] we have tested how the amount of noise affects to the measurement accuracy. As it may be noticed, despite adding noise up to the 75% of the pixels in the image (which is a very extreme case) the error remains low and stable both for the angle and distance. Again, these error values are in good agreement with those reported in Fig. 11 and we can deduce that the algorithm keeps an excellent performance under all these conditions. Despite the fact that the *S&P* pixels might be predominant, there are still a number of pixels defining a pattern that can be detected through the 2D-DFT.

Finally, the last case illustrates how the performance of the method is affected by the blurring of the image. It seems clear that it is not affected by it because the relative error remains low, stable, and again in the error range obtained in Fig. 11 for ideal C-scans with the same characteristics. We deduce that blurring effects reduce the resolution of an image but, as long as it does not change the main patterns present, they can still be detected by the 2D-DFT.

With these results, it is seen that the proposed approach is robust against experimental noise and blurring, even in highly affected cases. Only a big dispersion in the intensity of the noise can hinder the detection of the smallest patterns in some cases.

4. Conclusions

In this work, we have described an image processing methodology that enables the visualization and quantitative measurement of the woven fabrics in GFRP. The method mainly consists of concatenating fast and straightforward averaging, binarization, filtering techniques, and Fourier analysis. It leads to an accurate representation of the composite's reinforcement microstructure from a raw C-scan THz image.

The algorithm has been demonstrated on real composite samples, in this case a 2/2 twill weave reinforcing a polyamide matrix. The analysis has succeeded in characterizing the microstructure-induced process, which resulted in an average bundles' orientation of -44.52° and 41.61° and distances of 4.05 and 3.86 mm at the surface ply. These results are in excellent agreement with the manufacturer's information and reveal imperfect alignment induced by the thermo-compression process.

Furthermore, the utility of this approach in extracting information on the inner structure of these laminates has been corroborated. Thanks to the combination of the penetration capability of THz waves and signal/image processing, the orientation and spacing of the fibers at different plies has been determined, despite the lower SNR, revealing that the misalignment of one of the directions persists in depth. The error induced by the image processing algorithms has been quantified: It is less than 3% for the distance and within 2%–8% for the angle. The proposed algorithm has additionally demonstrated strong capabilities to deal with blurred or noisy raw images without any meaningful increase in the measurement error. Moreover, the robustness of the method and the values optimized for each variable has been demonstrated, as the accuracy is excellent even when a batch of artificially generated C-scans with a wide range of characteristics has been analyzed.

In conclusion, this work reports for the first time the measurement, in the different plies, of the characteristics of the woven fabric of laminated GFRP by a THz image-based method. The described method is of potential interest for the NDE of GFRP composites and opens the door to be used in a more versatile way for extracting quantitative information of the sample for quality control or in situations where the woven fabrics might be distorted. Specifically, the approach presented here gives accurate quantitative information on the weave's tow orientations and spatial period. This information may be helpful to determine whether materials have been fabricated to specification or damaged in service.

Author statement

J. Calvo-de la Rosa: Methodology, Software, Formal analysis, Investigation, Writing – Original Draft, Visualization. P. Pomarède: Methodology, Writing – Review & Editing, Validation.

P. Antonik: Conceptualization, Writing – Review & Editing, Supervision, Project administration, Funding acquisition.

F. Meraghni: Resources, Writing – Review & Editing, Project administration, Funding acquisition.

D.S. Citrin: Conceptualization, Resources, Writing – Review & Editing, Supervision, Project administration, Funding acquisition.

D. Rontani: Conceptualization, Writing – Review & Editing, Supervision, Project administration, Funding acquisition.

A. Locquet: Conceptualization, Resources, Writing – Review & Editing, Supervision, Project administration, Funding acquisition.

Declaration of competing interest

The authors declare that they have no known competing financial interests or personal relationships that could have appeared to influence the work reported in this paper.

Data availability

The data that has been used is confidential.

Acknowledgements

JCR, PA, DR, AL, and DSC gratefully acknowledge the financial support of the Conseil Régional du Grand Est, of the Fonds Européen de Développement Régional (FEDER), of the Institut Carnot ARTS, and of CPER SusChemProc. DR gratefully acknowledges the support of the Chair in Photonics. FM and PP would like to thank Stellantis for their support in the framework of the OpenLab Materials and Processes involving Stellantis group, Arts et Métiers (ENSAM) and Georgia Tech-Europe. They are grateful to DuPont de Nemours for providing the materials of this study.

References

[1] Soutis CA. Fibre Reinforced Composites Aircraft construction 2005;41:143–51. https://doi.org/10.1016/j.paerosci.2005.02.004.

[2] Wang Q, Li X, Chang T, Zhang J, Liu L, Zhou H, Bai J. Nondestructive imaging of hidden defects in aircraft sandwich composites using terahertz time-domain spectroscopy. Infrared Phys Technol 2019;97:326–40. https://doi.org/10.1016/j.infrared.2019.01.013.

[3] Ospald F, Zouathi W, Beigang R, Matheis C, Recur B, Guillet J, Mounaix P, Bosom PV, Ospald F, Zouathi W, Beigang R, Matheis C, Jonuscheit J, Ospald F, Zouaghi W, Beigang R, Matheis C, Jonuscheit J, Recur B. Aeronautics composite material inspection with a terahertz time-domain spectroscopy system to cite this version : HAL Id : hal-00942971 Aeronautics composite material inspection with a terahertz time-domain spectroscopy system. 2014. 0–14.

[4] Becker F, Hopmenn C, Italiano F, Girelli A. Fatigue testing of GFRP materials for the application in automotive leaf springs. Procedia Struct Integr 2019;19:645–54. https://doi.org/10.1016/j.prostr.2019.12.070.

[5] Sinha M, Tyagi RK. Strength and corrosion analysis in alloy steel and E-glass composite wear ring in automotive engine cooling water pump. Mater Today Proc 2020;21:1474–8. https://doi.org/10.1016/j.matpr.2019.11.054.

[6] Yang R, He Y, Zhang H. Progress and trends in nondestructive testing and evaluation for wind turbine composite blade. Renew Sustain Energy Rev 2016;60:1225–50. https://doi.org/10.1016/j.rser.2016.02.026.

[7] Jensen JP, Skelton K. Wind turbine blade recycling : experiences , challenges and possibilities in a circular economy. Renew Sustain Energy Rev 2018;97:165–76. https://doi.org/10.1016/j.rser.2018.08.041.

[8] Zhang S, Caprani CC, Heidarpour A. Strain rate studies of pultruded glass fibre reinforced polymer material properties : a literature review. Construct Build Mater 2018;171:984–1004. https://doi.org/10.1016/j.conbuildmat.2018.03.113.

[9] Fang H, Bai Y, Liu W, Qi Y, Wang J. Connections and structural applications of fi bre reinforced polymer composites for civil infrastructure in aggressive environments. Compos. Part B 2019;164:129–43. https://doi.org/10.1016/j.compositesb.2018.11.047.

[10] Khan MA, Kumar AS. Machinability of glass fibre reinforced plastic (GFRP) composite using alumina-based ceramic cutting tools. J Manuf Process 2011;13:67–73. https://doi.org/10.1016/j.jmapro.2010.10.002.

[11] Callister WD. Materials science and engineering. seventh ed. John Wiley & Sons, Inc.; 2007. https://doi.org/10.1007/BF01184995.

[12] Karbhari VM, editor. Non-destructive evaluation (NDE) of polymer matrix composites. first ed. Woodhead Publishing; 2013.

[13] Miqoi N, Pomarède P, Meraghni F, Declercq NF, Guillaumat L, Le Coz G, Delalande S. Detection and evaluation of barely visible impact damage in woven glass fabric reinforced polyamide 6.6/6 composites using ultrasonic imaging , X-ray tomography and optical profilometry. Int J Damage Mech 2020:1–26. https://doi.org/10.1177/1056789520957703.

[14] Eckel S, Meraghni F, Pomarède P, Declercq NF. Investigation of damage in composites using nondestructive nonlinear acoustic spectroscopy. Exp Mech 2017;57. https://doi.org/10.1007/s11340-016-0222-6.

[15] Cristofani E, Friederich F, Wohnsiedler S, Matheis C, Jonuscheit J, Vandewal M, Beigang R. Nondestructive testing potential evaluation of a terahertz frequency-modulated continuous-wave imager for composite materials inspection. Opt Eng 2014;53:031211. https://doi.org/10.1117/1.oe.53.3.031211.

[16] Dai B, Wang P, Wang TY, You CW, Yang ZG, Wang KJ, Liu JS. Improved terahertz nondestructive detection of debonds locating in layered structures based on wavelet transform. Compos Struct 2017;168:562–8. https://doi.org/10.1016/j.compstruct.2016.10.118.

[17] Zhang X, Guo Q, Chang T, Cui HL. Broadband stepped-frequency modulated continuous terahertz wave tomography for non-destructive inspection of polymer materials. Polym Test 2019;76:455–63. https://doi.org/10.1016/j.polymertesting.2019.04.001.

[18] Dong J, Kim B, Locquet A, McKeon P, Declercq NF, Citrin DS. Nondestructive evaluation of forced delamination in glass fiber-reinforced composites by terahertz and ultrasonic waves. Compos B Eng 2015;79:667–75. https://doi.org/10.1016/j.compositesb.2015.05.028.

[19] Dong J, Locquet A, Declercq NF, Citrin DS. Polarization-resolved terahertz imaging of intra- and inter-laminar damages in hybrid fi ber-reinforced composite laminate subject to low-velocity impact. Compos B Eng 2016;92:167–74. https://doi.org/10.1016/j.compositesb.2016.02.016.

[20] Han DH, Kang LH. Nondestructive evaluation of GFRP composite including multi-delamination using THz spectroscopy and imaging. Compos Struct 2018;185:161–75. https://doi.org/10.1016/j.compstruct.2017.11.012.

[21] Jördens C, Scheller M, Wietzke S, Romeike D, Jansen C, Zentgraf T, Wiesauer K, Reisecker V, Koch M. Terahertz spectroscopy to study the orientation of glass fibres in reinforced plastics. Compos Sci Technol 2010;70:472–7. https://doi.org/10.1016/j.compscitech.2009.11.022.

[22] Albrecht K, Baur E, Endres HJ, Gente R, Graupner N, Koch M, Neudecker M, Osswald T, Schmidtke P, Wartzack S, Webelhaus K, Müssig J. Measuring fibre orientation in sisal fibre-reinforced, injection moulded polypropylene – pros and cons of the experimental methods to validate injection moulding simulation. Compos. Part A Appl Sci Manuf 2017;95:54–64. https://doi.org/10.1016/J.COMPOSITESA.2016.12.022.

[23] Park DW, Oh GH, Kim HS. Predicting the stacking sequence of E-glass fiber reinforced polymer (GFRP) epoxy composite using terahertz time-domain spectroscopy (THz-TDS) system. Compos B Eng 2019;177:107385. https://doi.org/10.1016/j.compositesb.2019.107385.

[24] Tang C, Tanabe T, Yudate S, Oyama Y. Quantitative evaluation of fiber structure by using coherent terahertz wave. Compos B Eng 2019;159:1–3. https://doi.org/10.1016/J.COMPOSITESB.2018.08.135.

[25] Wang Q, Zhou H, Liu M, Li X, Hu Q. Study of the skin depth and defect detection in carbon fiber composites with Terahertz waves. Optik 2019;178:1035–44. https://doi.org/10.1016/j.ijleo.2018.09.162.

[26] Xu J, Wang H, Duan Y, He Y, Chen S, Zhang Z. Terahertz imaging and vibro-thermography for impact response in carbon fiber reinforced plastics. Infrared Phys Technol 2020;109:103413. https://doi.org/10.1016/j.infrared.2020.103413.

[27] Dong J, Pomarède P, Chehami L, Locquet A, Meraghni F, Declercq NF, Citrin DS. Visualization of subsurface damage in woven carbon fiber-reinforced composites using polarization-sensitive terahertz imaging. NDT E Int 2018;99:72–9. https://doi.org/10.1016/j.ndteint.2018.07.001.

[28] Pomarède P, Meraghni F, Peltier L, Delalande S, Declercq NF. Damage evaluation in woven glass reinforced polyamide 6 . 6/6 composites using ultrasound phase-shift analysis and X-ray tomography. J Nondestr Eval 2018;37. https://doi.org/10.1007/s10921-018-0467-3.

[29] Russ JC. The image processing handbook. fifth ed. Taylor & Francis; 2002.

[30] Gonzalez RC, Woods RE. Digital image processing. fourth ed. Essex: Pearson Global Edition; 2018.

[31] scikit-image, scikit-image. image processing in python. 2020.

[32] Broughton SA, Bryan K. Discrete fourier analysis and wavelets. Wiley; 2009.

[33] Marquez JP. Fourier analysis and automated measurement of cell and fiber angular orientation distributions. Int J Solid Struct 2006;43:6413–23. https://doi.org/10.1016/j.ijsolstr.2005.11.003.

[34] Zhai M, Locquet A, Roquelet C, Alexandre P, Daheron L, Citrin DS. Nondestructive measurement of mill-scale thickness on steel by terahertz time-of-flight tomography. Surf Coating Technol 2020;393:125765. https://doi.org/10.1016/j.surfcoat.2020.125765.

[35] Zhai M, Locquet A, Roquelet C, Citrin DS. Terahertz time-of-flight tomography beyond the axial resolution limit: autoregressive spectral estimation based on the modified covariance method. J Infrared, Millim Terahertz Waves 2020;41:926–39. https://doi.org/10.1007/s10762-020-00722-1.

[36] Zhai M, Locquet A, Roquelet C, Ronqueti LA, Citrin DS. Thickness characterization of multi-layer coated steel by terahertz time-of-flight tomography. NDT E Int 2020;116:102358. https://doi.org/10.1016/j.ndteint.2020.102358.

[37] Zhai M, Locquet A, Citrin DS. Pulsed THz imaging for thickness characterization of plastic sheets. NDT E Int 2020;116:102338. https://doi.org/10.1016/j.ndteint.2020.102338.
[38] Nguyen NQ, Mehdikhani M, Straumit I, Gorbatikh L, Lessard L, Lomov SV. Micro-CT measurement of fibre misalignment: application to carbon/epoxy laminates manufactured in autoclave and by vacuum assisted resin transfer moulding. Compos. Part A Appl Sci Manuf 2018;104:14–23. https://doi.org/10.1016/j.compositesa.2017.10.018.
[39] Malcom AJ, Aronson MT, Wadley HNG. Three-dimensionally woven glass fiber composite struts : characterization and mechanical response in tension and compression. J Compos Mater 2016;50:25–43. https://doi.org/10.1177/0021998315569751.